ACS Catalysis

# FIB-SEM Tomography Probes the Mesoscale Pore Space of an Individual Catalytic Cracking Particle

D. A. Matthijs de Winter, Florian Meirer, and Bert M. Weckhuysen*

Inorganic Chemistry and Catalysis Group, Debye Institute for Nanomaterials Science, Utrecht University, Universiteitsweg 99, 3584 CG Utrecht, The Netherlands

S Supporting Information

ABSTRACT: The overall performance of a catalyst particle strongly depends on the ability of mass transport through its pore space. Characterizing the three-dimensional structure of the macro- and mesopore space of a catalyst particle and establishing a correlation with transport efficiency is an essential step toward designing highly effective catalyst particles. In this work, a generally applicable workflow is presented to characterize the transport efficiency of individual catalyst particles. The developed workflow involves a multiscale characterization approach making use of a focused ion beam-scanning electron microscope (FIB-SEM). SEM imaging is performed on cross sections of 10.000 μm^2, visualizing a set of catalyst particles, while FIB-SEM tomography visualized the pore space of a large number of 8 μm^3 cubes (subvolumes) of individual catalyst particles. Geometrical parameters (porosity, pore connectivity, and heterogeneity) of the material were used to generate large numbers of virtual 3D volumes resembling the sample's pore space characteristics, while being suitable for computationally demanding transport simulations. The transport ability, defined as the ratio of unhindered flow over hindered flow, is then determined via transport simulations through the virtual volumes. The simulation results are used as input for an upscaling routine based on an analogy with electrical networks, taking into account the spatial heterogeneity of the pore space over greater length scales. This novel approach is demonstrated for two distinct types of industrially manufactured fluid catalytic cracking (FCC) particles with zeolite Y as the active cracking component. Differences in physicochemical and catalytic properties were found to relate to differences in heterogeneities in the spatial porosity distribution. In addition to the characterization of existing FCC particles, our method of correlating pore space with transport efficiency does also allow for an up-front evaluation of the transport efficiency of new designs of FCC catalyst particles.

KEYWORDS: fluid catalytic cracking, focused ion beam-scanning electron microscopy, diffusion simulation, porous media, upscaling, transport ability
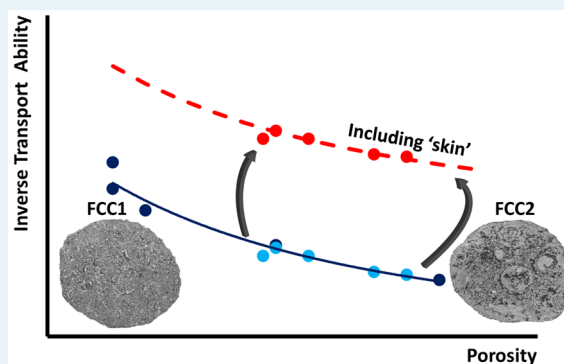
1. INTRODUCTION

The performance of a heterogeneous catalyst is governed by the complex interplay between the available pore space and the embedded catalytically active sites.[1−4] Reactant molecules travel through the pore space of a heterogeneous catalyst particle toward the catalytically active sites to undergo reaction, followed by the transport of the product molecules to the catalyst particle outer surface.[5] Typical diameters of the size of this pore space range, according to the IUPAC definitions, from macropores (>50 nm) via mesopores (2−50 nm) to micropores (<2 nm).[6] The accessibility, or ability for reactant and product molecules to travel through the pore space, is of key importance to the overall activity and selectivity of a catalyst material, hence acquiring fundamental knowledge on the pore space of a catalytic solid is of high importance to researchers working in both academia and chemical industries.[3,7−9]

Recent advances in analytical methods have enabled the visualization in three dimensions of the pore space of catalyst materials. X-ray nanotomography is able to resolve pore volumes of entire catalyst particles with a real 3D resolution of ~100−300 nm, down to a real 3D resolution of ~139 nm for small subvolumes of the particles.[4,10−15] A recent example is a X-ray nanotomography study on the effects of metal deposition on a single fluid catalytic cracking (FCC) particle with respect to macropore clogging.[11] Another method includes focused ion beam-scanning electron microscopy (FIB-SEM), which can resolve in steamed zeolite crystal mesopores down to ~5 nm in diameter,[16] while transmission electron microscopy (TEM) resolves even mesopores down to ~2 nm in, for example, thin slices of zeolite powders.[17]

Without 3D visualization techniques, transport modeling is based on continuum models[18,19] or statistical models.[18,20] The main challenge, however, remains in accurately characterizing the complex pore structure with a limited number of

parameters.[21] Direct visualization of the pore space of a catalyst particle offers the opportunity for quantitative determination of the geometrical parameters, such as local pore distributions,[22] the pore size distribution,[23] tortuosity and constrictivity,[24,25] and general principles of percolation theory, e.g. via multidirectional pore-network models.[26] The correlation between such geometrical parameters and the material's mass transport ability has been an active scientific topic for over a century.[25,27] One of the remaining challenges is incorporating an accurate description of the hierarchical complex heterogeneous pore space. While geometrical parameters are useful for assigning classes of porous materials, the predictive capability of geometrical parameters for the ability to transport mass without fitting parameters remains ambiguous:[28,29] for example, when tortuosity is considered.[30,31]

In this work we present a generally applicable workflow. In conjunction with microcontinuum models[21] we foresee that the workflow allows for multiscale modeling of reaction-diffusion processes. In the present work, through the workflow, we provide novel insights into the bulk transport properties of individual macro- and mesoporous catalyst particles, on the basis of a detailed multiscale characterization study using the FIB-SEM method. The studied catalyst particles are used in fluid catalytic cracking (FCC). The FCC process is generally considered as the workhorse of current oil refineries as it produces, next to gasoline, an important fraction of the propylene used for making plastics.[4,32]

The spherical FCC particles have an average diameter of 50–150 μm, consisting of several components, such as zeolite, clay, alumina, and silica. The feedstock molecules, such as high-molecular-weight aromatics and naphthenes most often found in the naphtha fraction of crude oil, travel through the matrix, i.e. within the macro- and mesopores, while undergoing precracking, before entering the micropores of the embedded zeolite crystals. Acidic sites within the zeolite's crystalline framework perform the actual cracking process.[32] The efficiency of the FCC particle is determined by the intraparticle (matrix) and intracrystalline (zeolite) transport ability,[33] with the intraparticle transport ability qualitatively linked to the accessibility of the zeolite component.[7,34]

We investigated two sets of industrially manufactured FCC catalyst particles containing zeolite Y, further referred to as FCC1 and FCC2. The main properties of both catalyst materials are summarized in Table 1, while further details on these materials can be found in previous articles from our group.[3,35] Scanning electron microscopy (SEM) images reveal two distinct appearances (Figure 1), corresponding to different manufacturing processes. The "skin" around FCC2 provides a strong attrition resistance, but at the expense of the transport ability into the particles.[36] A reduction in the transport ability is suggested by the pore accessibility index, as given in Table 1, which is a relative measure of the initial penetration rate of large nonreactant organic molecules into the FCC particle pore space.[37] In addition, as evidenced in Table 1, the catalytic cracking conversion efficiency is distinctly lower for FCC2 than for FCC1. Unfortunately, the transport ability through FCC particles cannot be derived quantitatively from the nitrogen physisorption and mercury macroporosity experiments performed. Table 1 clearly shows the differences in mean surface area and porosity for both FCC catalyst materials, but no actual pore space morphology can be deduced.[25]

The developed workflow consists of four phases (Figure 2) and allows characterizing and correlating the three-dimensional structure of the macro- and mesopore space of catalyst particles to its transport properties, taking FCC catalyst particles as a showcase.

Starting with the original spherical particle, phase I is the measurement of the two-dimensional spatial porosity distribution using grids of squares with fixed dimensions applied to thresholded high-resolution SEM images. Phases II and III are executed in parallel with phase I. Phase II is the characterization of the macro- and mesopore space in small ($2 \times 2 \times 2 \ \mu m^3$) arbitrarily chosen subvolumes of the sample obtained by FIB-SEM tomography. Transport simulations (finite element steady-state diffusion) through the subvolumes are computationally expensive. Therefore, phase III applies an algorithm to simulate these subvolumes in the form of virtual volumes, which can be processed by standard desktop computers. Percolation (0 or 1) is determined from a large number of virtual volumes, and an average percolation value (between 0 and 1) is calculated as a function of the porosity of the virtual volumes, defining a percolation probability (PP). Likewise, transport ability values resulting from transport simulations through the virtual volumes are plotted against their porosity value. From this relationship we want to obtain a continuous distribution of transport ability values (y axis) for every porosity value (x axis). Therefore, the transport ability is described mathematically by a probability distribution function with the mean and standard deviation as a function of the porosity. Finally, phase IV combines the percolation probability and the transport ability distribution from phase III and the spatial porosity distribution from phase I into an upscaling scheme, applying an analogue of electrical resistor networks. As a result of this approach, the transport through (cubic) volumes with equal dimensions as the original FCC particles can be simulated on the basis of the determined macro- and mesopore space. From these results we were then able to provide an explanation for the observed differences in physicochemical and catalytic properties between FCC1 and FCC2, as summarized in Table 1.

Table 1. Physicochemical Properties, Pore Accessibility Indexes, and Catalytic Performances of the Two Sets of Industrially Manufactured Fluid Catalytic Cracking (FCC) Materials, Denoted as FCC1 and FCC2, under Investigation[a]

	FCC1	FCC2
(N_2) BET surface area (m^2/g)	230	253
(N_2) micropore volume (cm^3/g)	0.055	0.079
(Hg) total intrusion volume (mL/g)	0.32	0.28
(Hg) total pore area (m^2/g)	79.5	26.2
mean pore diameter (volume) (nm)	59.5	177.0
pore accessibility index	10.2	2.3
430 °F+ conversion (wt %)	73	69

[a]They contain zeolite Y as the active cracking component.

2. TRANSPORT SIMULATIONS

Transport through FCC particles is generally described as a diffusion process.[33] Using Fick's diffusion law, the dimensionless transport ability σ is defined for steady-state flow conditions as a ratio of flows:

$$\frac{1}{\sigma} = \frac{\Phi_0}{\Phi_m} = \frac{D_0}{D_m} \frac{A_0}{A_m} \frac{L_m}{L_0} = \frac{D_0}{D_m} \frac{\tau_m}{\varepsilon_m} \quad (1)$$
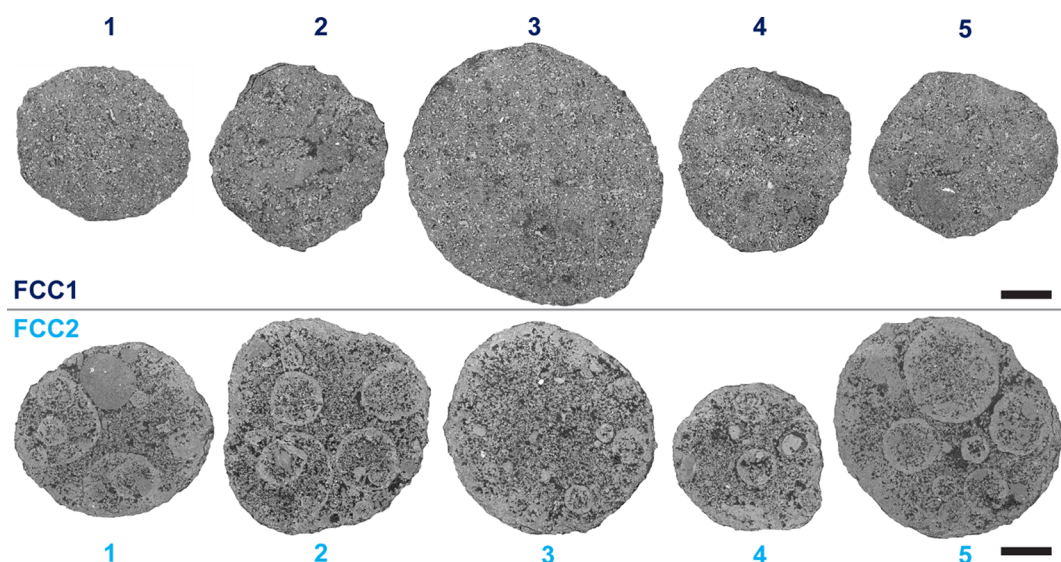
Figure 1. Selection of cross sections of the two sets of fluid catalytic cracking (FCC) particles under study: FCC1 and FCC2. The scale bars are 25 μm.
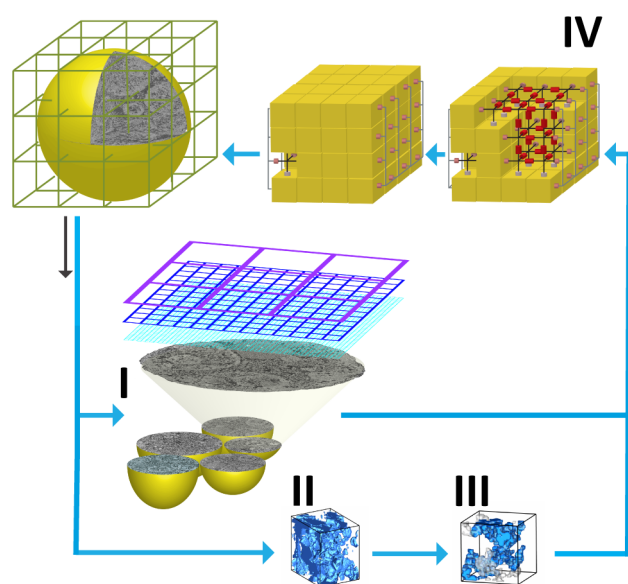

Figure 2. Multiscale workflow, starting from the top left. Phase I involves measurement of the two-dimensional spatial porosity distribution for squares with varying dimensions applied to thresholded high-resolution SEM images. Phases II and III are executed in parallel with phase I. Phase II, characterization of the macro- and mesopore space in small $(2 \times 2 \times 2 \ \mu m^3)$ FCC subvolumes obtained by FIB-SEM. Phase III, algorithm to mimic the FCC subvolumes as virtual volumes, which are suitable for flow simulations. On the basis of a large number of flow simulations, the transport ability is plotted as a function of porosity. The scatter plot can be mathematically described by a probability distribution function. In addition, a percolation probability is established as a function of porosity. Phase IV combines the percolation probability, the transport ability distribution, and the spatial porosity distribution into an upscaling scheme, which uses an analogue of electrical resistor networks.
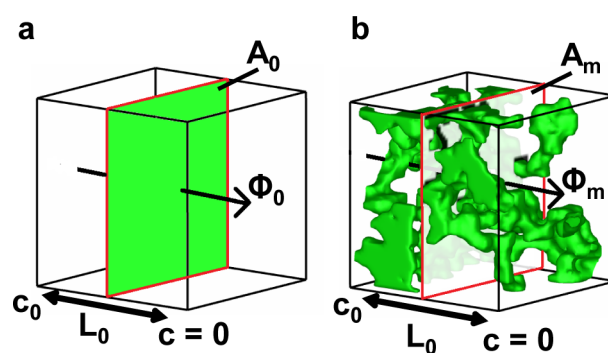

Figure 3. (a, b) Transport ability, defined as the ratio of the unhindered flow Φ_0 and the simulated or measured flow Φ_m through the porous volume. (b) Example of a virtual volume generated by the snake algorithm method.

Furthermore, L_m, τ_m, and ε_m are the effective length, the effective tortuosity, and the effective porosity, respectively, as discussed below.

In the case of Knudsen diffusion, the ratio D_0/D_m becomes $\neq 1$. Knudsen diffusion is in effect when the ratio between pore radii and the mean free path is smaller than 0.1. A ratio greater than 10 is considered sufficient for pure stochastic diffusion. A transition regime exists between ratios of 10 and 0.1, where both bulk diffusion and Knudsen diffusion are combined.[38,39] In the case of naphthalene, assuming a molecular diameter of ~0.6 nm,[40] a pressure of 300 kPa, and a temperature of 500 K,[32] the mean free path is estimated to be ~14 nm, while the pore dimensions are typically on the order of tens of nanometers (the resolving power in our work is $20 \times 20 \times 20 \ nm^3$). Although the workflow in principle would be capable of dealing with Knudsen diffusion, in practice the chosen setup would require significant changes. Furthermore, we are currently aiming for a qualitative comparison between FCC1 and FCC2, rather than a quantitative comparison with the bulk sample measurements (Table 1). Therefore, Knudsen diffusion is currently ignored, resulting in $D_0/D_m = 1$.

In eq 1, the measured flow is then defined by an effective cross section A_m (m^2) and an effective length L_m (m). The

where Φ_0 (mol s^{-1}) is the unrestricted flow through a volume with cross section A_0 (m^2) and length L_0 (m), and Φ_m (mol s^{-1}) is the "measured" or simulated flow through the same volume (A_0L_0) (Figure 3). D_0 $(m^2 \ s^{-1})$ is the diffusion constant of the gas, and D_m $(m^2 \ s^{-1})$ is an effective diffusion constant.

ratios A_0/A_m and L_m/L_0 result in an effective porosity ε_m and an effective tortuosity τ_m. Much effort is put into establishing an explicit universal correlation between the transport ability and geometrical parameters.[25,41] Specifically, a correlation is sought among D_m, ε_m, and τ_m. The applicable definitions for ε_m and τ_m vary, adding complexity to the quest.[32] Defining transport ability as a ratio of flows implies incorporating the geometrical parameters without explicitly separating for example ε_m and τ_m, simplifying the relation between geometrical parameters and the transport ability.

An advantage of our definition of the transport ability is the potential for a direct comparison between experimental and theoretical results. Of eminent importance for our approach is the required steady state, posing constraints on experiments.[28] A comparison of steady-state flow conditions with equilibrated systems[42] requires detailed knowledge of the actual pore space geometry. Dead-end pores are excluded from contributing to the flow for steady-state conditions but must be taken into account in equilibrated no-flow systems. As a consequence, correlating steady-state flow with equilibrated systems is not trivial.

In the actual FCC process, many different hydrocarbon species diffuse through the pores, fragments of cracked hydrocarbons, while many molecules are absorbed into and released from the zeolite domains.[4c,d] In addition, coke formation changes the entire pore space of the FCC particle during the process, restricting or completely blocking pores.[11,15b,c] In principle, a time-dependent transport ability parameter can be defined; however, modeling such a time-dependent dynamic process across relevant length scales is currently beyond the scope of the current research.

3. RESULTS AND DISCUSSION

3.1. Spatial Porosity Distribution Measurements of Fluid Catalytic Cracking Catalyst Particles (Phase I).

Figure 1 shows the SEM images of the FCC1 and FCC2 catalyst particles, which were recorded with a scan resolution of ~6 nm. The SEM images were thresholded for the porosity. The resolution does not allow for imaging of the micropores within the zeolite domains. Therefore, the total porosity of the FCC particles on the basis of the SEM images will not compare to bulk analyses: e.g., nitrogen physisorption. The resolution is sufficient to determine the meso- and macroporosity.

In the following, grids consisting of squares with dimensions of 2×2, 8×8, or 32×32 μm^2 were applied for each individual FCC particle and the porosity was determined for each individual square as the ratio of pore area over the total area. For details we refer to Figure S1 in the Supporting Information. From the collection of porosity values (from 2×2, 8×8, or 32×32 μm^2 squares), a mean and standard deviation was calculated, resulting in a table required for phase IV: i.e., the upscaling routine.

3.2. Pore Space Characterization of Subvolumes of Fluid Catalytic Cracking Particles (Phase II).

FIB-SEM tomography[16] and digital postanalysis resulted in 243 FCC subvolumes of $2 \times 2 \times 2$ μm^3 (56 × FCC1; 187 × FCC2), visualizing the pore space with a spatial resolution of $20 \times 20 \times 20$ nm. Each FCC subvolume consists of a series of 100 images of 253×320 pixels.

With a spatial resolution of $20 \times 20 \times 20$ nm, micropore space was not taken into account. Therefore, the flow through the zeolite domains is ignored. Transport into, out of, and through zeolite domains are important rate-limiting steps for a

complete description of the FCC process.[19] In the present work, we are interested in the overall transport through FCC particles. As transport through zeolite domains is very slow,[43] we neglect its contribution to the overall percolation (section 3.4) and transport. The selected spatial resolution and postprocessing are such that percolation of the $2 \times 2 \times 2$ μm^3 FCC subvolumes through the meso- and macropores is accurately preserved (visual inspection). It is important to note that not all pore space in one subvolume is interconnected. Isolated pore space ("not-connected") was distinguished from the "connected" pore space. For details of the analysis methods we refer to the Supporting Information. Examples of the three-dimensional pore space reconstruction for individual FCC subvolumes are shown in Figure 4 and Figure S3 in the Supporting Information.
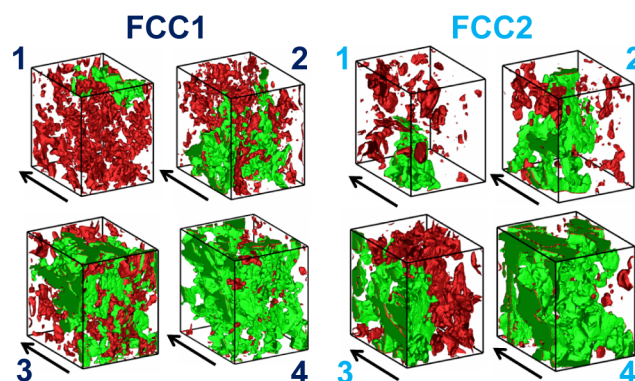

Figure 4. Examples of the reconstructed macro- and mesopore spaces of FCC1 and FCC2 subvolumes of $2 \times 2 \times 2$ μm^3. Transport is assumed to occur in one direction, indicated by the arrows, while the sides are considered closed, the percolating pore space is displayed in green, and the isolated pore space is displayed in red. The numbering corresponds to the numbers in Figures 5 and 6b.

To execute phase III, i.e. creating virtual volumes, two geometrical parameters were measured: (1) the connected porosity versus the total porosity and (2) the heterogeneity of the pore space within each FCC subvolume. On consideration of the heterogeneity, after identification of the connected pore space, each FCC subvolume was split back into the original 100 separate images. The standard deviation of the connected porosity values found in all 100 images is considered as a measure of the heterogeneity within the corresponding FCC subvolume.

The connected porosity is plotted as a function of the total porosity, and the heterogeneity of the pore space of individual FCC subvolumes is plotted as a function of their corresponding connected porosities (Figure 5a,b). Both scatter plots indicate strong similarities between the pore space of FCC1 and FCC2 at a $2 \times 2 \times 2$ μm^3 scale. The similarity enables the use of a single algorithm for generating a pore space in a virtual volume, representative for both FCC1 and FCC2, which is phase III.

3.3. Virtual Volumes of a Fluid Catalytic Cracking Particle (Phase III).

Simulating diffusion through the measured FCC subvolumes is computationally expensive. Therefore, small virtual volumes ($50 \times 50 \times 50$ voxels) were generated, using two different algorithms: (1) a stochastic distribution of pore space throughout the virtual volume, referred to as the "random algorithm", and (2) a random walk-like algorithm, referred to as the "snake algorithm". Both the random algorithm and the snake algorithm are able to generate
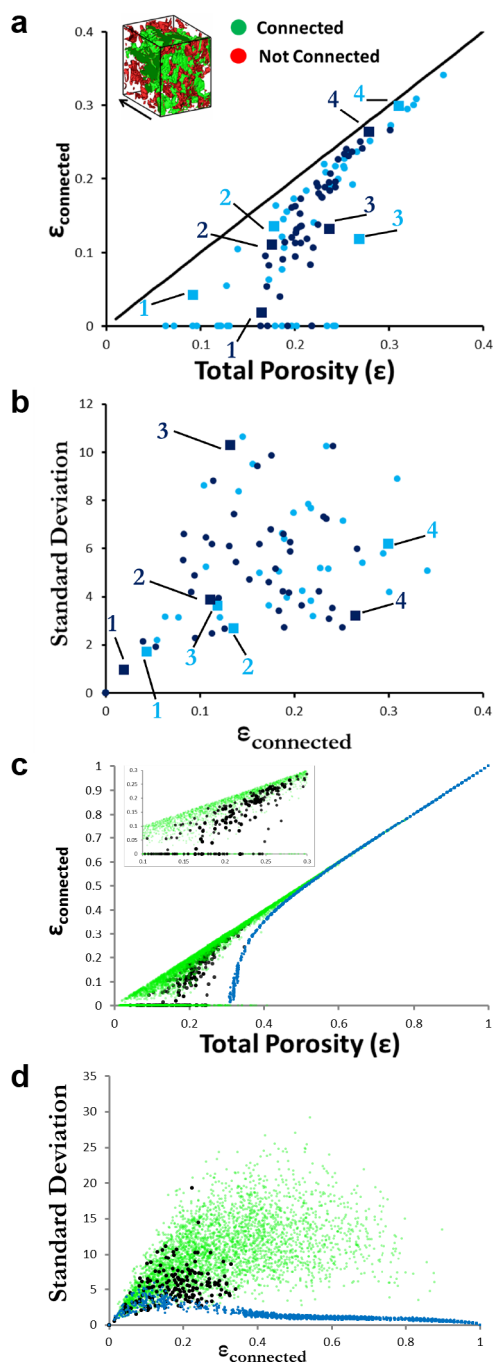
Figure 5. Characterization of the pore space geometries and a comparison between the FCC subvolumes and the virtual volumes. (a) Scatter plot of the connected porosity and the total porosity (50 × FCC1; 50 × FCC2). The dark and light blue data points indicate data from FCC1 and FCC2, respectively. The numbering corresponds to Figure 4. (b) Same as (a), comparing the standard deviation of connected porosity of the FCC subvolumes. (c, d) Comparison between the FCC subvolumes (dark data points, 243 subvolumes) and the virtual volumes generated by the random algorithm (blue data points) and the snake algorithm (green data points).

isolated pore space by using periodic boundary conditions. For details we refer to the Supporting Information. An example of a virtual volume generated by the snake algorithm is shown in Figure 3b.

A total of 9462 virtual volumes was generated (4334 × random; 5128 × snake) and were compared with the measured

FCC subvolumes (FCC1 and FCC2 combined) for the connected porosity and for the heterogeneity of the pore space, as found in phase II (Figure 5c,d).

The geometrical properties (connected porosity, heterogeneity of the pore space) of the virtual volumes, generated by the snake algorithm, are found to be comparable to the geometrical properties of the FCC subvolumes by visual inspection. As a result, transport ability will be determined through virtual volumes generated by the snake algorithm.

3.4. Percolation Probability and Transport Ability Distribution (Phase III). A volume is either percolating (percolation = 1) or not percolating (percolation = 0). Percolation was determined for 10.000 virtual volumes and plotted against the porosity of each of the virtual volumes. The porosity range (0−1) is split into intervals of 0.02, and from each interval the average percolation is calculated. The result is defined as the percolation probability (PP) (Figure 6a; a plot of the square root of the percolation probability). For details we refer to the Supporting Information.

In order to find the transport ability, flow through percolating virtual volumes was simulated by a finite element method, solving Fick's second law for all voxels, using the
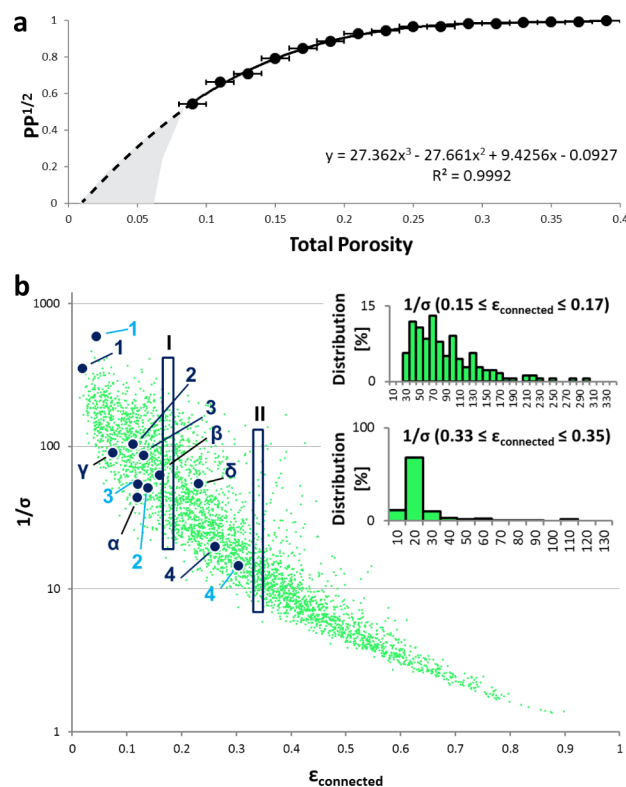

Figure 6. (a) Square root of the percolation probability (PP), determined from virtual volumes generated by the snake algorithm. The horizontal bars indicate the binning step ($\Delta\varepsilon$ = 0.02) of the moving average. The curve is fitted to the data points (0.09 ≤ ε ≤ 0.39). The percolation probability is one for porosities larger than 0.4. The percolation probability for ε < 0.09 is rapidly decreasing to 0, as indicated by the gray area. (b) Scatter plot of the transport ability for the percolating virtual volumes generated by the snake algorithm. The numbers correspond to the numbers in Figures 4 and 5, indicating the transport ability determined for FCC subvolumes. FCC2 subvolumes $\alpha-\delta$ are shown in Figure S3 in the Supporting Information. The insets show the skewed distribution of the inverse of the transport ability σ^{-1} for a specific porosity range.

Jacobi (iterative) method, which establishes the concentration levels throughout the pore volumes. The boundary conditions were as follows: fixed concentration levels at the entrance (c_0) and exit ($c = 0$) plane, while the four remaining boundary planes of a cube were closed to transport (Figure 3a,b). When the solution of the partial differential equation of each voxel becomes stable, i.e. no more (significant) changes in concentration levels throughout the volume are observed, steady-state conditions are obtained and Φ_m is calculated. Steady-state flow was considered when the difference between $\Phi_{z=0}$ and $\Phi_{z=L_0}$ became negligible (0.01% of the concentration difference between the entrance and exit planes).

In this way the transport ability σ was determined for 5128 percolating virtual volumes generated by the snake algorithm and is plotted versus the connected porosity in Figure 6b. For comparison, the transport ability of the 12 measured FCC subvolumes (4 × FCC1; 8 × FCC2) is plotted, indicating a similar scatter.

Our scatter plot for the transport ability resembles the scatter plots found for permeability of porous media.[44] Other work, based on experimental evidence[28] and computer simulations,[29] argued that a "simple and unique relationship" between the transport ability and geometrical parameters does not exist, although such a relationship is often suggested in the literature.[25,41] To capture the transport ability in a mathematical framework, rather than an explicit equation, we propose to describe a specific porous material by a probability distribution function for the inverse of the transport ability $F(\sigma^{-1})$. (Note that, since we explicitly account for percolation, we avoid the numerical issue of σ being 0.) The insets in Figure 6b show two histograms of $1/\sigma$ for regions I and II of the connected porosity. Despite the skewed distribution, a standard deviation and mean can be calculated, defining the probability distribution for the inverse transport ability as $\sigma^{-1} \approx N(a,b^2)$, where $a(\varepsilon_{connected})$ and $b(\varepsilon_{connected})$ are the mean and standard deviation, respectively. It was found that, when the whole data set was examined, both $a(\varepsilon_{connected})$ and $b(\varepsilon_{connected})$ are best fitted by an exponential function with a polynomial as exponent (Table S1 in the Supporting Information).

With a mathematical description for the percolation probability, the transport ability distribution, and the corresponding spatial porosity distribution for the FCC samples in place, it becomes possible to generate their values in an upscaling routine, which does not require further full-scale simulation efforts.

3.5. Upscaling Routine for Translating the Properties of the Set of Virtual Volumes into a Transport Ability of a Catalyst Particle (Phase IV). The upscaling routine combines a number of virtual volumes into a larger cube of $n \times n \times n$ virtual volumes. On the basis of the spatial porosity distribution found in phase I, the porosity of each of the $n \times n \times n$ virtual volumes is assigned using a Gaussian random generator. Subsequently, a random generator determines whether or not the virtual volume is percolating, on the basis of the assigned porosity and the percolation probability (Figure 6a). Finally, a transport ability value is assigned to the percolating virtual volumes using another Gaussian random generator, based on the assigned porosity and $F(\sigma^{-1})$ as found in phase III.

Then the transport ability of the whole cube of $n \times n \times n$ virtual volumes is calculated using the analogue of an electrical

resistor network.[45] Instead of using the transport ability, we now define a transport resistance R:

$$R = \frac{c_0}{\Phi_m} = \frac{L_0}{D_0 A_0} \frac{1}{\sigma} \tag{2}$$

assuming $c(L_0) = 0$ (Figure 3a). The advantage of using a transport resistance is the availability of the mathematics as applied to electrical circuitries.

Therefore, the cube of $n \times n \times n$ virtual volumes is translated into a three-dimensional resistor network, as shown in Figure 2. Each resistor value is calculated from the average inverse transport ability value of both neighboring virtual volumes. Nodes from nonpercolating virtual volumes are taken out of the network, as well as isolated nodes. Subsequently, an equivalent resistor value is calculated for the network by Gaussian-Jordan elimination.[46] From the equivalent resistor value, a transport ability for the $n \times n \times n$ virtual volumes is calculated (eq 2).

Calculating the transport ability of a sufficient number of $n \times n \times n$ virtual volumes results in a new scatter plot of the inverse transport ability as a function of the average porosity of the $n \times n \times n$ virtual volumes. Nonpercolating virtual volumes are considered nonporous. Now a new distribution probability function $F_2(\sigma^{-1})$ is fitted and can be used for a second upscaling step.

The upscaling routine, as described above, can be repeated until the dimensions of the original object are obtained, as illustrated in Figure 2.

The current implementation of the upscaling routine implies two assumptions. (1) No interfacial boundary exists between two neighboring virtual volumes: i.e., pores are likely to be continuous from one virtual volume to another. As in practice no pore space is generated for the upscaling routine, the first assumption is somewhat trivial.

The second assumption is related, assuming (2) that the overall percolation probability remains unaffected when percolating virtual volumes are placed in series. This second assumption is likely to require a future refinement. Although each percolating volume contains a pathway through the volume, the pathways through the consecutive volumes may not be connected. Volumes placed in series result in a percolation probability of less than 1, especially for small porosity values. An example from FCC2 subvolumes is shown in Figure S3 in the Supporting Information. However, for simplicity, percolation is considered to be unaffected by the potential discontinuity of pathways. In support of the simplification is the 3D nature of the upscaling routine, increasing the probability of percolation.

For each upscaling step, the transport ability was calculated for 10.000 cubes. The virtual volumes generated by the snake algorithm (phase III) represent $2 \times 2 \times 2$ μm^3 FCC subvolumes (phase II). Therefore, the spatial porosity distribution (phase I) was determined for 2×2 μm^2 squares.

Upscaling is performed with cubes of $4 \times 4 \times 4$ virtual volumes, resulting in a transport ability scatter plot, representative for volumes of $8 \times 8 \times 8$ μm^3.

From the scatter plot, a new distribution probability function $F(\sigma^{-1})$ is derived. For all particles and all upscaling steps, an exponential equation was found to fit best, strongly resembling Archie's empirical law, which describes flow through porous media.[47] The fitting parameters used are described in Table S2 in the Supporting Information.

The upscaling routine was repeated with another $4 \times 4 \times 4$ volume, repeating phase I with 8×8 μm^2 squares, resulting in a transport ability scatter plot representative for volumes of $32 \times 32 \times 32$ μm^3. As shown in Figure 2, a final upscaling step is performed with $3 \times 3 \times 3$ volumes, resulting in a transport ability scatter plot representative for volumes of $96 \times 96 \times 96$ μm^3, close to the FCC diameters.

The upscaling scatter plots for FCC1 and FCC2 are shown in Figure 7 and Figure S4 in the Supporting Information. The tables included in the figures provide the input data from phase I, the porosity distribution.
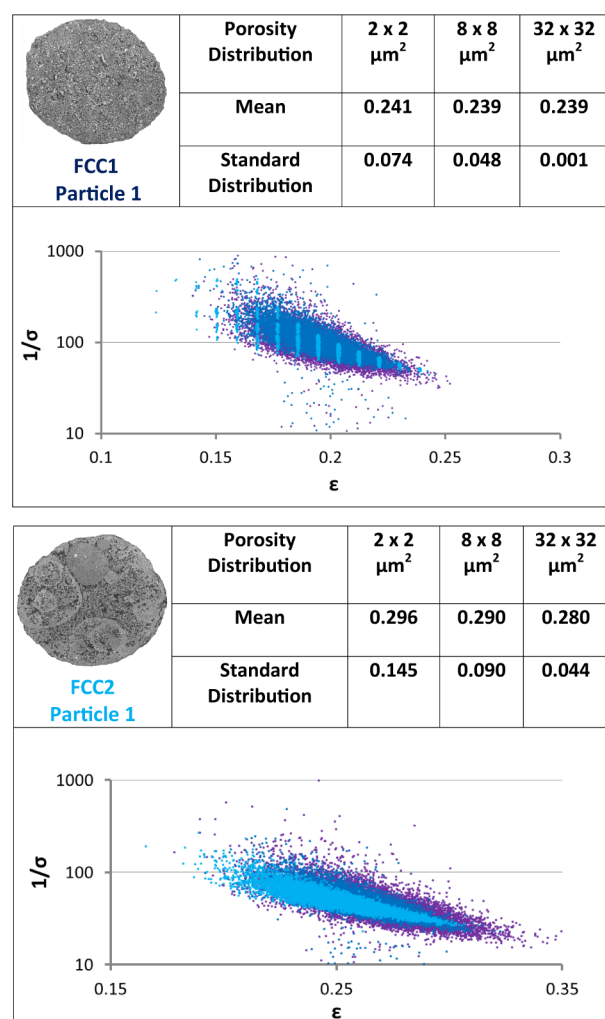
Porosity Distribution	2 x 2 μm^2	8 x 8 μm^2	32 x 32 μm^2
Mean	0.241	0.239	0.239
Standard Distribution	0.074	0.048	0.001

FCC1 Particle 1

Porosity Distribution	2 x 2 μm^2	8 x 8 μm^2	32 x 32 μm^2
Mean	0.296	0.290	0.280
Standard Distribution	0.145	0.090	0.044

FCC2 Particle 1

Figure 7. Upscaling routine for the FCC1 (Figure 1, particle 1) and FCC2 (Figure 1, particle 1) particles. The fitting parameters for the consecutive steps can be found in the Supporting Information. The purple data points are the result of the first upscaling step. The dark blue and light blue data points are the result of the second and third upscaling steps, respectively. The mean and standard deviation values are obtained from the 2D SEM porosity measurements. For a clear display, the horizontal scales in the graphs are not equal. See also Figure S4 in the Supporting Information.

The first upscaling step for FCC1 (purple data points, Figure 7 and Figure S4 in the Supporting Information) shows a horizontal scatter around the mean porosity value of 0.241, reflecting the heterogeneity across the entire FCC1 particle. The horizontal scatter for the FCC2 particle (Figure 7 and Figure S4) is significantly wider. Visually (Figure 1 and Figure

S1 in the Supporting Information), the FCC2 particle is more heterogeneous than the FCC1 particle, which results in approximately twice the value of the standard deviation for the porosity.

Due to the use of random generators, a few outliers (approximately 0.5%) are found at small values for the inverse transport ability ($1/\sigma$). Because of the small number of occurrences, these outliers are ignored.

The second upscaling step (dark blue data points, Figure 7 and Figure S4 in the Supporting Information) resulted in a narrower horizontal scatter, due to a reduced heterogeneity, a trend continued by the third upscaling step (light blue data points, Figure 7 and Figure S4). The heterogeneity of FCC1 for the last upscaling step is close to 0 (the standard deviation is 0.001).

As a consequence, all of the virtual volumes ($32 \times 32 \times 32$ μm^3) were assigned with almost equivalent porosity values. It is the percolation probability that is effectively changing the porosity, as nonpercolating virtual volumes are assigned with a 0 porosity value. As a result of the discretization of space, the overall porosity of the volume makes a noticeable step with each virtual volume being nonpercolating (light blue data points, Figure 7 (FCC1) and Figure S4 in the Supporting Information). The effect occurs for all upscaling steps but is only noticeable in the case of a very small standard deviation of the porosity.

3.6. Comparison among the Transport, Physicochemical, and Catalytic Properties of FCC Catalyst Particles. The upscaling routine has been applied to the 10 FCC particles ($5 \times$ FCC1; $5 \times$ FCC2) from Figure 1, and the resulting inverse transport ability values are plotted versus the corresponding overall porosities (Figure 8a). Contrary to expectations, on the basis of the pore accessibility index in Table 1, the average transport ability of FCC2 is greater than the transport ability of FCC1 (Figure 8a: the average *inverse* transport ability of FCC2 is smaller than the *inverse* transport ability of FCC1). However, not yet taken into account was the presence of the "skin" around the FCC2 particles. In a final step, following again the analogue of electrical resistors, the FCC2 particles were therefore represented by a single resistor value, while the "skin" was represented by a sheet of parallel resistors (Figure 8b). On the basis of the SEM images (Figure 1), the "skin" has an estimated thickness of 2 μm; therefore, the characteristics of the $2 \times 2 \times 2$ μm^3 volumes were applicable for determining the parameters of the parallel resistors. The "skin" was found to have an estimated porosity of 0.07, again based on the 2D SEM data, which is very close to the percolation threshold (Figure 6a). Nevertheless, the fitted equation is used to calculate the percolation probability of 0.19.

The FCC2 bulk resistor represents a volume of $96 \times 96 \times 96$ μm^3. The combined $2 \times 2 \times 2$ μm^3 volumes and the percolation probability result in sheets of $48 \times 48 \times 0.019 = 437$ parallel resistors for each plane. The mean inverse transport ability ($\varepsilon = 0.07$) is 160 (Table S1 in the Supporting Information), which results in a transport resistance value of 80 per resistor (according to eq 2). Therefore, the sheets of parallel resistors have an equivalent transport resistance of 0.18.

The bulk transport resistance of FCC2 varies from 0.18 to 0.26. The combination of the equivalent transport resistance of the "skin" and the FCC2 bulk transport resistance results in a significant increase in inverse transport ability (Figure 8c). Consequently, the transport properties of FCC2 are significantly poorer than the transport properties of FCC1.
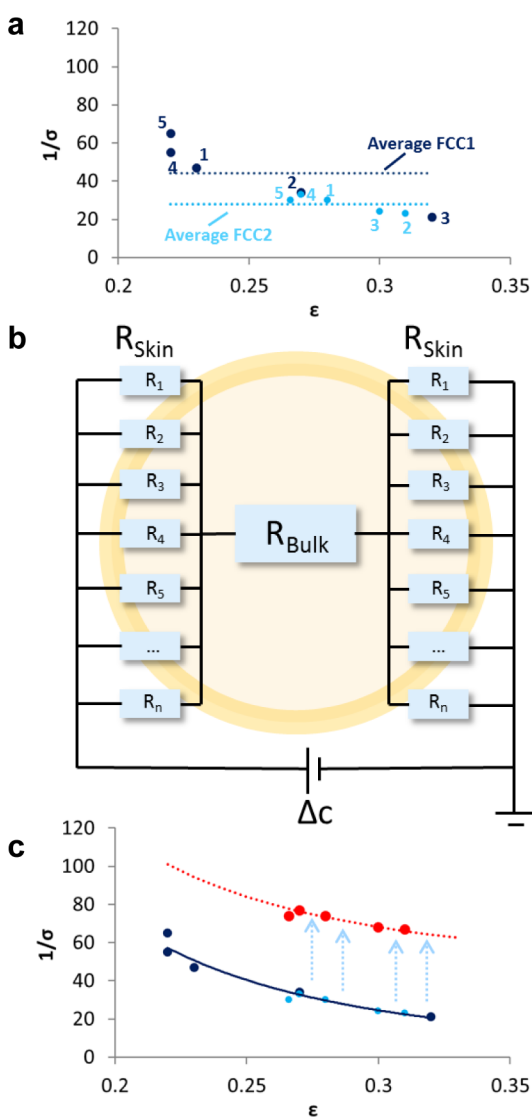
Figure 8. (a) Result from upscaling the five particles from FCC1 and the five particles from FCC2, shown in Figure 1. The numbering of the data points corresponds to the numbering in Figure 1 and Figure S4 in the Supporting Information. Also shown is the average over the five particles for both types. The internal structure of FCC2 causes less hindrance to mass transport. (b) The "skin" of FCC2, represented by a sheet of parallel resistors, with the FCC interior being represented by a single resistance value. (c) Addition of the "skin" resulting in a significant difference between FCC1 and FCC2, in favor of FCC1 in terms of transport ability or efficiency.

The presence of the "skin" can explain the contradiction between the lower accessibility and the large mean pore diameter for FCC2 (Table 1), as the interior of the FCC2 has a significantly higher porosity (Figure 1 and Figure S1 in the Supporting Information), but the access to the interior is restricted by the "skin". Therefore, the large pores present in FCC2 do not contribute to the initial uptake. This observation is consistent with FCC1 having a lower overall porosity and a smaller mean pore diameter but higher accessibility (see Table 1).

To improve the accessibility of FCC2, adding a few parallel resistors with a small resistance value to the sheet of parallel resistors (Figure 8b) would have a significant impact of the overall or equivalent resistance. Considering the "skin" of

FCC2, one or more highly porous volumes of $2 \times 2 \times 2 \ \mu m^3$ in the "skin" would completely overcome the limiting effect of the "skin", provided the entire pore space behind the "skin" is interconnected. This insight offers opportunities for the design of improved FCC particles with a high attrition resistance.

4. CONCLUSIONS

We have developed a generally applicable multiscale workflow for exploring the macro- and mesoscale pore space of an individual catalyst particle in a qualitative manner. The approach is based on the use of a focused ion beam-scanning electron microscope (FIB-SEM) and tested for two distinct types of industrially manufactured fluid catalytic cracking (FCC) particles (FCC1 and FCC2) containing zeolite Y as active material as showcases of multicomponent and hierarchically structured catalyst materials. Both catalyst materials clearly differ in their overall pore accessibility and catalytic performances, as outlined in Table 1.[35] The first part of the developed workflow characterizes porosity in 2D from $100 \times 100 \ \mu m^2$ areas with 6 nm pixel resolution and in 3D volumes of $2 \times 2 \times 2 \ \mu m^3$ with 20 nm resolving power, using the FIB-SEM. The second part of the developed workflow is upscaling, translating relevant characteristics of the $2 \times 2 \times 2 \ \mu m^3$ volumes to the bulk properties of catalyst particles.

The designed and tested methodology was able to explain the differences in pore accessibility and related catalytic performances (Table 1) between the two types of FCC particles, as found by bulk characterization measurements, including nitrogen and mercury porosimetry.[35] Despite a larger BET surface area and a larger mean pore diameter for FCC2 in comparison with FCC1, the pore accessibility index is lower, as well as the conversion rate. Through the combination of 2D and 3D analyses and the upscaling workflow, we have shown that the denser "skin" (surface layer) of FCC2 plays an important role in the reduction of accessibility and in turn the conversion rates. Considering the near-surface, pore-clogging metal accumulation during the lifetime of the FCC particles,[11,15b−d] the presence of such a "skin" is likely to enhance the effect of pore blocking by metal deposition and therefore accelerate the deactivation of the FCC2 particles in comparison with FCC1. Potentially, pore blocking rapidly diminishes the advantage of the proposed highly porous entrances through the "skin" in FCC2, suggesting a number larger than one or two highly porous volumes is required for a consistent improvement of the accessibility during the lifetime of the FCC2 particles. Innovations in the design of the porosity distribution and the "skin" and time-dependent structural changes can be directly implemented in the developed mathematical framework, helping to design catalyst materials with improved mass transport properties that remain stable over longer time periods.

Our work shows that heterogeneity occurs at different length scales within a single catalyst particle. In addition, the recent work of Remi et al.[48] demonstrated considerable differences of mass transfer into nanoporous materials such as the zeolite domains, as well as between different nanoporous materials. Although working with larger volumes reduces catalyst particle heterogeneities, e.g. by using representative elemental volumes, a thorough understanding of the processes and dynamics must take into account these multiscale heterogeneities. We believe a distribution function would be a native representation of a complex arbitrary pore structure, as opposed to an explicit equation with multiple fitting parameters, in particular when

the distribution function is based on 3D visualization techniques. Consequently, microcontinuum models[19,21] could need to be adapted to accommodate the proposed distribution function in order to model an entire FCC riser reactor, allowing a direct link between catalyst design and its effects for the FCC riser reactor yield. Such lines of thought could be the basis for future research work.

■ ASSOCIATED CONTENT

Ⓢ Supporting Information

The Supporting Information is available free of charge on the ACS Publications website at DOI: 10.1021/acscatal.6b00302.

> Additional information concerning the experimental results as well as the technical descriptions and instrumentation used (PDF)

■ AUTHOR INFORMATION

Corresponding Author

*E-mail for B.M.W.: b.m.weckhuysen@uu.nl.

Notes

The authors declare no competing financial interest.

■ ACKNOWLEDGMENTS

■ REFERENCES

(1) (a) *Handbook of Heterogeneous Catalysis*; Ertl, G., Knozinger, H., Schüth, F., Weitkamp, J., Eds.; Wiley-VCH: Weinheim, Germany, 2008. (b) Thomas, J. M.; Thomas, W. J. *Principles and Practice of Heterogeneous Catalysis*; Wiley-VCH: Weinheim, Germany, 2014. (c) Hagen, J. *Industrial Catalysis, A Practical Approach*; Wiley-VCH: Weinheim, Germany, 2006.

(2) Mitchell, S.; Michels, N. L.; Kunze, K.; Perez-Ramirez, J. *Nat. Chem.* **2012**, *4*, 825−831.

(3) (a) Weckhuysen, B. M. *Angew. Chem., Int. Ed.* **2009**, *48*, 4910−4943. (b) Buurmans, I. L. C.; Weckhuysen, B. M. *Nat. Chem.* **2012**, *4*, 873−886.

(4) (a) Rase, H. F. *Handbook of Commercial Catalysts*; CRC Press: New York, 2000. (b) Sadeghbeigi, R. *Fluid Catalytic Cracking Handbook, an Expert Guide to the Practical Operation, Design, and Optimization of FCC Units*, 3rd ed.; Butterworth-Heinemann: Oxford, U.K., 2002. (c) Vogt, E. T. C.; Weckhuysen, B. M. *Chem. Soc. Rev.* **2015**, *44*, 7342−7370. (d) Vogt, E. T. C.; Whiting, G. T.; Dutta Chowdhury, A.; Weckhuysen, B. M. *Adv. Catal.* **2015**, *58*, 143−314.

(5) Deutschmann, O.; Knözinger, H.; Kochloefl, K.; Turek, T. Heterogeneous Catalysis and Solid Catalysts. *Ullmann's Encyclopedia of Industrial Chemistry*; Wiley: Hoboken, NJ, 2009.

(6) Rouquerol, J.; Avnir, D.; Fairbridge, C. W.; Everett, D. H.; Haynes, J. H.; Pernicone, N.; Ramsay, J. D. F.; Sing, K. S. W.; Unger, K. K. *Pure Appl. Chem.* **1994**, *66*, 1739−1758.

(7) Dupain, X.; Makkee, M.; Moulijn, J. A. *Appl. Catal., A* **2006**, *297*, 198−219.

(8) Grunwaldt, J.-D.; Wagner, J. B.; Dunin-Borkowski, R. E. *ChemCatChem* **2013**, *5*, 62−80.

(9) Kärger, J.; Binder, T.; Chmelik, C.; Hibbe, F.; Krautscheid, H.; Krishna, R.; Weitkamp, J. *Nat. Mater.* **2014**, *13*, 333−343.

(10) Ruiz-Martínez, J.; Beale, A. M.; Deka, U.; O'Brien, M. G.; Quinn, P. D.; Mosselmans, J. F. W.; Weckhuysen, B. M. *Angew. Chem., Int. Ed.* **2013**, *52*, 5983−5987.

(11) Meirer, F.; Morris, D. T.; Kalirai, S.; Liu, Y.; Andrews, J. C.; Weckhuysen, B. M. *J. Am. Chem. Soc.* **2015**, *137*, 102−105.

(12) Grunwaldt, J.-D.; Schroer, C. G. *Chem. Soc. Rev.* **2010**, *39*, 4741−4753.

(13) Bare, S. R.; Charochak, M. E.; Kelly, S. D.; Lai, B.; Wang, J.; Chen-Wiegart, Y. K. *ChemCatChem* **2014**, *6*, 1427−1437.

(14) Da Silva, J. C.; Mader, K.; Holler, M.; Haberthür, D.; Diaz, A.; Guizar-Sicairos, M.; Cheng, W.-C.; Shu, Y.; Raabe, J.; Menzel, A.; Van Bokhoven, J. A. *ChemCatChem* **2015**, *7*, 413−416.

(15) (a) Price, S. W. T.; Ignatyev, K.; Geraki, K.; Basham, M.; Filik, J.; Vo, N. T.; Witte, P. T.; Beale, A. M.; Mosselmans, J. F. W. *Phys. Chem. Chem. Phys.* **2015**, *17*, 521−529. (b) Meirer, F.; Kalirai, S.; Morris, D.; Soparawalla, S.; Liu, Y.; Mesu, G.; Andrews, J. C.; Weckhuysen, B. M. *Sci. Adv.* **2015**, *1*, e1400199. (c) Meirer, F.; Kalirai, S.; Weker, J. N.; Liu, Y.; Andrews, J. C.; Weckhuysen, B. M. *Chem. Commun.* **2015**, *51*, 8097−8100. (d) Wise, A. M.; Weker, J. N.; Kalirai, S.; Farmand, M.; Shapiro, D. A.; Meirer, F.; Weckhuysen, B. M. *ACS Catal.* **2016**, *6*, 2178−2181.

(16) (a) Karwacki, L.; De Winter, D. A. M.; Aramburo, L. R.; Lebbink, M. N.; Post, J. A.; Drury, M. R.; Weckhuysen, B. M. *Angew. Chem., Int. Ed.* **2011**, *50*, 1294−1298. (b) Aramburo, L. R.; Karwacki, L.; Cubillas, P.; Asahina, S.; De Winter, D. A. M.; Drury, M. R.; Buurmans, I. L. C.; Stavitski, E.; Mores, D.; Daturi, M.; Bazin, P.; Dumas, P.; Thibault-Starzyk, F.; Post, J. A.; Anderson, M. W.; Terasaki, O.; Weckhuysen, B. M. *Chem. - Eur. J.* **2011**, *17*, 13773−13781.

(17) (a) Koster, A. J.; Ziese, U.; Verkleij, A. J.; Janssen, A. H.; De Jong, K. P. *J. Phys. Chem. B* **2000**, *104*, 9368−9370. (b) Midgley, P. A.; Dunin-Borkowski, R. E. *Nat. Mater.* **2009**, *8*, 271−280. (c) Friedrich, H.; De Jongh, P. E.; Verkleij, A. J.; De Jong, K. P. *Chem. Rev.* **2009**, *109*, 1613−1629. (d) Arslan, I.; Walmsley, J. C.; Rytter, E.; Bergene, E.; Midgley, P. A. *J. Am. Chem. Soc.* **2008**, *130*, 5716−5719. (e) Zecevic, J.; De Jong, K. P.; De Jongh, P. E. *Curr. Opin. Solid State Mater. Sci.* **2013**, *17*, 115−125.

(18) Sahimi, M.; Gavalas, G. R.; Tsotsis, T. *Chem. Eng. Sci.* **1990**, *45*, 1443−1502.

(19) Bidabehere, C. M.; Garcia, J. R.; Sedran, U. *Chem. Eng. Sci.* **2015**, *137*, 293−300.

(20) Kikkinides, E. S.; Politis, M. G. *Adsorption* **2014**, *20*, 5−20.

(21) Steefel, C. I.; Beckingham, L. E.; Landrot, G.; Steefel, C. I.; Emmanuel, S.; Anovitz, L. M. Pore-scale geochemical processes. *Rev. Mineral. Geochem.* **2015**, *80*, 217−246.

(22) Hilfer, B. *Phys. Rev. B: Condens. Matter Mater. Phys.* **1991**, *44*, 60−75.

(23) Münch, B.; Holzer, L. *J. Am. Ceram. Soc.* **2008**, *91*, 4059−4067.

(24) Gommes, C. J.; Bons, A.-J.; Blacher, S.; Dunsmuir, J. H.; Tsou, A. H. *AIChE J.* **2009**, *55*, 2000−2012.

(25) Gaiselmann, G.; Neumann, M.; Schmidt, V.; Pecho, O.; Hocker, T.; Holzer, L. *AIChE J.* **2014**, *60*, 1983−1999.

(26) Raoof, A.; Nick, H. M.; Hassanizadeh, S. M.; Spiers, C. J. *Comput. Geosci.* **2013**, *61*, 160−174.

(27) Knudsen, M. *Ann. Phys.* **1909**, *333*, 75−130.

(28) Bruckler, L.; Ball, B. C.; Renault, P. *Soil Sci.* **1989**, *147*, 1−10.

(29) Liu, G.; Li, B.; Hu, K.; Van Genuchten, M. Th. *Soil Sci. Soc. Am. J.* **2006**, *70*, 1252−1261.

(30) Clennell, M. B. *Geol. Soc. Spec. Publ.* **1997**, *122*, 299−344.

(31) Ghanbarian, B.; Hunt, A. G.; Ewing, R. P.; Sahimi, M. *Soil Sci. Soc. Am. J.* **2013**, *77*, 1461−1477.

(32) Rigutto, M. In *Zeolites and Catalysis: Synthesis, Reactions and Applications*; Cejka, J., Corma, A., Zones, S., Eds.: Wiley-VCH: Weinheim, Germany, 2010; pp 547−584.

(33) O'Connor, P.; Verlaan, J. P. J.; Yanik, S. J. *Catal. Today* **1998**, *43*, 305−313.

(34) Kuehler, C. W.; Jonker, R.; Imhof, P.; Yanik, S. J.; O'Connor, P. *Stud. Surf. Sci. Catal.* **2001**, *134*, 311−322.

(35) (a) Buurmans, I. L. C. Ph.D. Dissertation, Utrecht University, 2011. (b) Buurmans, I. L. C.; Ruiz-Martínez, J.; Knowles, W. V.; Van der Beek, D.; Bergwerff, J. A.; Vogt, E. T. C.; Weckhuysen, B. M. *Nat. Chem.* **2011**, *3*, 862−867. (c) Buurmans, I. L. C.; Soulimani, F.; Ruiz-Martinez, J.; van der Bij, H. E.; Weckhuysen, B. M. *Microporous Mesoporous Mater.* **2013**, *166*, 86−92. (d) Karreman, M. A.; Buurmans, I. L. C.; Geus, J. W.; Agronskaia, A. V.; Ruiz-Martinez, J.; Gerritsen, H. C.; Weckhuysen, B. M. *Angew. Chem., Int. Ed.* **2012**, *51*, 1428−1431. (e) Karreman, M. A.; Buurmans, I. L. C.; Agronskaia, A. V.; Geus, J. W.; Gerritsen, H. C.; Weckhuysen, B. M. *Chem. - Eur. J.* **2013**, *19*, 3846−3859.

(36) O'Connor, P.; Imhof, P.; Yanik, S. J. *Stud. Surf. Sci. Catal.* **2001**, *134*, 299−310.

(37) (a) Psarras, A. C.; Iliopoulou, E. F.; Nalbandian, L.; Lappas, A. A.; Pouwels, C. *Catal. Today* **2007**, *127*, 44−53. (b) Stamires, D.; O'Connor, P.; LaHeij, E. J.; Vadovic, C. U.S. Patent Application 20130203586 (A1), 2013.

(38) Pollard, W. G.; Present, R. D. *Phys. Rev.* **1948**, *73*, 762−774.

(39) Clifford, S. M.; Hillel, D. *Soil Sci.* **1986**, *141*, 289−297.

(40) Yu, Y.; Li, X.; Su, L.; Zhang, Y.; Wang, Y.; Zhang, H. *Appl. Catal., A* **2012**, *447-448*, 115−123.

(41) Shen, L.; Chen, Z. *Chem. Eng. Sci.* **2007**, *62*, 3748−3755.

(42) Kortunov, P.; Vasenkov, S.; Kärger, J.; Eliá, M. F.; Perez, M.; Stöcker, M.; Papdopoulos, G. K.; Theodorou, D.; Drescher, B.; McElhiney, G.; Bernauer, B.; Krystl, V.; Kocirík, M.; Zikánová, A.; Jirglová, H.; Berger, C.; Gläser, R.; Weitkamp, J.; Hansen, E. W. *Chem. Mater.* **2005**, *17*, 2466−2474.

(43) Pérez-Ramírez, J.; Christensen, C. H.; Egeblad, K.; Christensen, C. H.; Groen, J. C. *Chem. Soc. Rev.* **2008**, *37*, 2530−2542.

(44) Nelson, P. H. *Log Analyst* **1994**, *3*, 38−62.

(45) Schopper, J. R. *Geophys. Prospect.* **1966**, *14*, 301−341.

(46) Rink, M.; Schopper, J. R. *Geophys. Prospect.* **1968**, *16*, 277−294.

(47) Archie, G. E. *Trans. Am. Inst. Mining. Metallurg. Pet. Eng.* **1942**, *1476*, 54−61.

(48) Remi, J. C. S.; Lauerer, A.; Chmelik, C.; Vandendael, I.; Terryn, H.; Baron, G. V.; Denayer, J. F. M.; Kärger, J. *Nat. Mater.* **2015**, *15*, 401−406.